

Shape reconfiguration for underwater propeller efficiency improvement

Tristan Aurégan ¹, Sylvain Courrech du Pont ², and Benjamin Thiria¹

¹Laboratoire de *Physique et Mécanique des Milieux Hétérogènes*, PMMH UMR 7636 CNRS ESPCI PSL
Research University Univ. Paris-Diderot Sorbonne Université, Paris, France

²Laboratoire *Matière et Systèmes Complexes*, UMR CNRS 7057, Université Paris Cité, Paris, France



(Received 9 February 2024; accepted 21 May 2024; published 26 July 2024)

We investigate experimentally the propulsive efficiency of a propeller in water with chordwise flexible blades that deform under the action of fluid loading. Using a scale model experiment, we record the deformation of the blades as well as the thrust and torque generated by the rotor. The use of flexible materials can improve the resilience to changing external conditions: with optimal flexibility, the blades deform and remain efficient under off-design conditions. We derive a theoretical law for blade tip deformation and show good agreement with experiments. Our results suggest that, using only the blade flexibility alone, we are able to program the blade deformation to passively adopt an optimized shape for efficient propulsion within a given parameter range.

DOI: [10.1103/PhysRevFluids.9.074402](https://doi.org/10.1103/PhysRevFluids.9.074402)

I. INTRODUCTION

Flexible structures are often more resilient to fluctuations of external flow conditions. This property was first observed in nature by Vogel [1], who noticed that the leaves of the tulip tree change shape to adopt a more streamlined configuration in high-wind conditions. This ability to change shape is called reconfiguration and is common to many artificial or natural flexible systems. A large-amplitude shape change is associated with a modification of the loading from the surrounding fluid [2–6]. The streamlining of the body induces important changes in the flow field, causing a slower increase in fluid loading compared to the classical relationship for rigid bodies, which increases proportionally to the square of the flow velocity.

The coupling between fluid loading and deformation can also be used to improve performance. Many animal species benefit from fluid-structure interactions [7], either by using their fins in the case of fish and cetaceans, or their wings in the case of insects. In many instances, this deformation is associated with a modification of the propulsive efficiency [8,9]. Inspired by these examples, reconfiguration can be used in artificial systems to improve resilience to changes in external conditions. Cagnet *et al.* [10] used this principle by studying a wind turbine with flexible blades. The blades deform under the action of fluid loading and centrifugal force, and the authors show that using the right flexibility can extend the range over which a given wind turbine is efficient. The blades of the wind turbine passively change shape and adapt to external conditions (here, the wind velocity) in order to produce as much energy as possible.

Our goal in this study is to investigate the possibility of similarly extending the efficiency range of an underwater propeller. For this problem, it is the forcing from the rotation that causes both the loading and the deformation, and the centrifugal force plays a much smaller role than in the case of wind turbines.

Several studies have addressed the problem of flexibility in rotating systems: for instance, Sicard and Sirohi [11] and Mohd Zawawi *et al.* [12] studied highly flexible rotor blades in a microhelicopter configuration for safety or storage purposes. Wind turbines with flexible blades are widely studied in

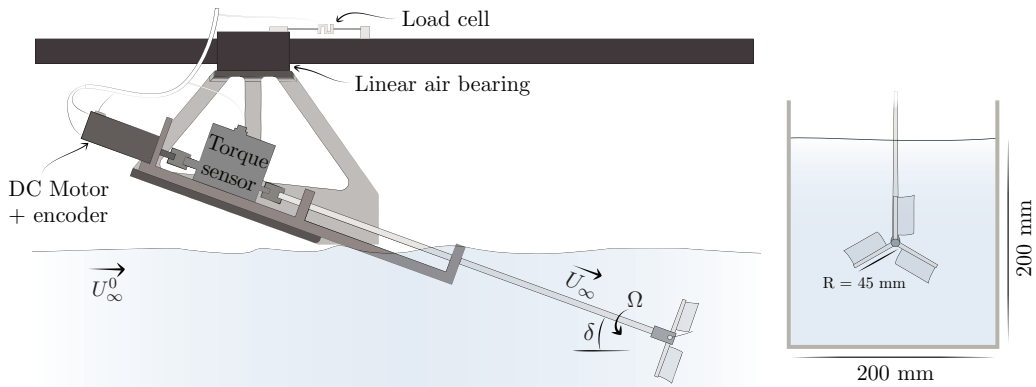


FIG. 1. Sketch of the experimental setup: side view (left) and downstream view (right).

the literature [13–16]; in particular, Cognet *et al.* [17] proposed an algorithm to find the appropriate blade material properties given a wind turbine geometry and a wind distribution to maximize the extracted energy.

Several efforts have also been made to theoretically describe the forces and deformations for flexible rotors [18–20]. In this article we use a similar description of the problem by dividing the blade into independent spanwise elements.

For propellers in water, the problem of flexibility has recently been studied on a model scale through the flow field around the rotor [21] or through the thrust produced [18]. In both studies, the propeller blade is fully flexible, allowing it to bend and twist under the action of the fluid. However, the bending deformation is always detrimental to thrust and efficiency as it reduces the area swept by the rotor. We therefore study a modified geometry with a rigid leading edge, so that only the twist deformation is allowed. Our goal is to study the propulsive efficiency of such a rotor and to investigate whether the use of a flexible blade can lead to a passive adaptation of the rotor to the flow conditions.

In this article, we first describe the experimental setup used to measure the efficiency of the rotors and then highlight the main parameters of the problem with a typical experiment. We show how the use of flexible blades improves the resilience to a change in external conditions and, finally, we derive a theoretical law for the deformation of the blade tip and compare it with experiments.

II. SETUP

We use a scale model boat to test the flexible bladed propellers. The boat is held in place above a free surface water channel and is tilted such that the propeller is submerged. The sensors and motor are placed above the free surface [Fig. 1(a)]. The boat is composed of a DC electric motor, a torque sensor, and a load cell. The DC electric motor rotates the shaft to which the propeller is attached. The torque sensor measures in real time the hydrodynamic torque required to rotate the propeller and the small parasitic torque associated with the two ball bearings used to hold the shaft in place. We measured this parasitic torque separately and removed it from the final torque measurement. The boat is attached to a carriage on a linear air bearing, itself held in place by a load cell. The linear air bearing only transmits the longitudinal force to the load cell that therefore measures the sum of the drag of the boat and the thrust generated by the propeller. We also measured the drag of both the hull and shaft without the propeller, which we subtract from the final thrust measurement. At last, we measure the angular velocity Ω , using a Hall effect sensor and a magnet attached to the rotating shaft that sends 25 pulses per revolution. The propeller is placed sufficiently deep in the water (100 mm from the top and bottom) and away from the channel walls so that there is no visible free surface effect from the propeller and the blockage remains limited (below 15%). It has to be

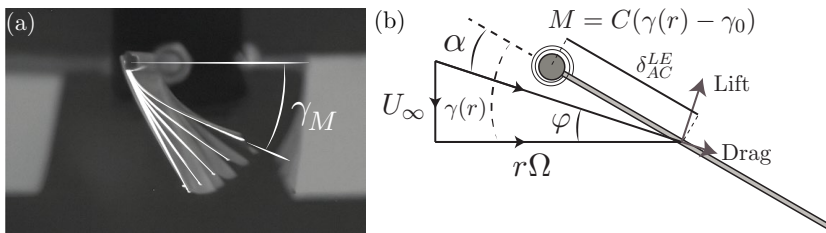


FIG. 2. (a) Superposition of pictures of the flexible propeller. The blade is illuminated by a laser sheet and several pictures with different angular velocities have been superimposed. As the angular velocity is increased, the deflection increases as well and the angle γ_M decreases. (b) Sketch of a radial cut of a blade at a distance r from the axis of rotation. The local velocity results from the combination of the angular velocity $r\Omega$ and the flow velocity U_∞ .

noted that the incoming flow on the blades is modified due to the angle δ of the propeller. Hence, the incoming velocity on the propeller, U_∞ , is the projection of the free stream velocity in the direction of the rotor: $U_\infty = U_\infty^0 \cos \delta$.

The propeller blades are made of three flexible plastic sheets glued to a rigid leading edge, all connected to a central hub. We introduce the pitch angle γ_0 of the blades as the angle between the undeformed blades and the plane of rotation. We use four flexible propellers labeled P1 through P4 from least to most flexible and one rigid propeller for the purpose of reference, which has blades made out of fiberglass. The blades have a maximum radius R , a minimal radius R_{\min} , and a chord c . (The mechanical properties of the blades are detailed in the Supplemental Material [22].)

The measurement protocol is defined as follows: the flow velocity is set by the variable-speed pump of the channel and the angular velocity of the rotor is increased in steps from 0 to 22 rad/s. Each step lasts 20 s and is repeated twice. In the following graphs, the shaded regions represent the fluctuation between repeated measurements. In parallel, a high-speed camera captures the shape of the blade at the tip. This camera is synchronized with the Hall effect sensor on the boat, taking 25 pictures per rotation of the propeller. The blade is illuminated by a laser sheet covering the entire chord at a given radius. The laser sheet is placed 1–2 mm from the tip, corresponding to 90% of the maximum radius. We then extract the images where the blade is facing the camera [Fig. 2(a)]. The tip twist angle $\gamma_M = \gamma(r = R)$ is measured from the images of the deformed blade using a Hough transform [23] to detect the main direction of the lit shape in the images. In practice, we measure the angle of the straight section near the trailing edge. The measurement is subsequently corrected because of the geometric bias introduced by the angle of the shaft. We focus on the deformation of the blade near the tip because the local velocity (and therefore the generated force) is the largest near the tip.

III. EXPERIMENTAL RESULTS

In order to compare the performance of the propeller between different operating conditions, we introduce the tip speed ratio,

$$\lambda = \frac{R\Omega}{U_\infty}, \quad (1)$$

with R the radius of the propeller, Ω the angular velocity, and U_∞ the incoming flow velocity, respectively.

For a given tip speed ratio, changing the flow velocity corresponds to a modification of the chord-based Reynolds number:

$$\text{Re} = \frac{R\Omega c}{\nu}, \quad (2)$$

with c the chord of the blades and ν the kinematic viscosity of water. In our case, Re ranges between 10^3 and 10^4 . High-Reynolds-number theory for flows around airfoils will therefore be used to characterize the flow dynamics.

Finally, the last relevant dimensionless parameter compares the flexibility of the material to the hydrodynamic loading. In this work, we consider the elasticity of the Mylar sheets as a pointwise torsional spring at the leading edge [Fig. 2(b)]. The material properties are therefore modeled as a single torsional spring per unit width C , measured using a bending test (the blades P1 through P4 have a torsional spring constant of 1.60×10^{-1} , 5.11×10^{-2} , 8.71×10^{-3} , and 2.32×10^{-3} N, respectively). The hydrodynamic loading on a blade profile per unit width scales as $1/2\rho c(R\Omega)^2$ and is applied at a typical distance c from the leading edge. Thus, we obtain a Cauchy number comparing the hydrodynamic moment on the leading edge to the restoring elastic force defined as follows:

$$C_Y = \frac{1/2\rho c^2(R\Omega)^2}{C}. \quad (3)$$

It has to be noted that the centrifugal force is negligible in this problem. This can be easily verified by considering a blade section located at a distance r from the axis of rotation. The forces per unit width exerted onto the section scale as

$$F_{\text{hydro}} \sim \rho c(R\Omega)^2, \quad F_{\text{centrifuge}} \sim \rho_{\text{blade}} R c e \Omega^2, \quad (4)$$

with ρ_{blade} the specific mass of the blade, and e its thickness. The ratio between the two reads

$$\frac{F_{\text{centrifuge}}}{F_{\text{hydro}}} \sim \frac{\rho_{\text{blade}}}{\rho} \frac{e}{R} \ll 1. \quad (5)$$

Thus, only three main dimensionless numbers (along with the pitch angle γ_0) are sufficient to characterize this system: the tip speed ratio λ , the Reynolds number Re , and the Cauchy number C_Y . Moreover, for high-Reynolds-number flows around airfoils, the Reynolds number is expected to have only negligible effects on both the lift and drag coefficients of the blade profile, and so on the generated forces. In consequence, changing the flow velocity while keeping a constant tip speed ratio will then only modify the Cauchy number. In the range of blade materials used, the Cauchy number spans more than three decades. For the sake of simplification, we hence kept the flow velocity constant throughout the study equal to $U_\infty^0 = 0.15$ m/s. Each blade flexibility can therefore be quantified using the number $C_Y/\lambda^2 = 1/2\rho c^2 U_\infty^2/C$. The blades P1 through P4 correspond to values of C_Y/λ^2 of 1.5×10^{-2} , 4.7×10^{-2} , 2.4×10^{-1} , and 1.0, respectively.

Figure 3 shows a typical example of the data obtained in an experiment, here for a pitch angle of $\gamma_0 = 60^\circ$. The blue curves correspond to the reference rigid propeller, and the data in the yellow to red shades correspond to increasingly flexible propellers. Four relevant quantities characterizing the performance of the rotor are plotted as a function of the tip speed ratio λ : the thrust and torque coefficients, defined as

$$C_T = \frac{T}{1/2\rho\pi R^2(R\Omega)^2}, \quad C_Q = \frac{Q}{1/2\rho\pi R^3(R\Omega)^2}, \quad (6)$$

with T and Q the hydrodynamic thrust and torque, respectively, the rotor efficiency η , and the tip twist angle γ_M . As can be observed, all the flexible blades produce less thrust than the rigid one [Fig. 3(a)] except for the least flexible ones. This can be understood considering the effect of the flexibility that reduces the twist angle on the blade [Fig. 3(d)] and aligns the blade with the local flow velocity. Under normal conditions of use, this results in a reduction in the lift generated and therefore in the thrust generated.

In this study, we are interested in the propulsive efficiency η , defined as the ratio between the useful power and the power expanded to spin the propeller:

$$\eta = \frac{TU_\infty}{Q\Omega} = \frac{C_T}{\lambda C_Q}. \quad (7)$$

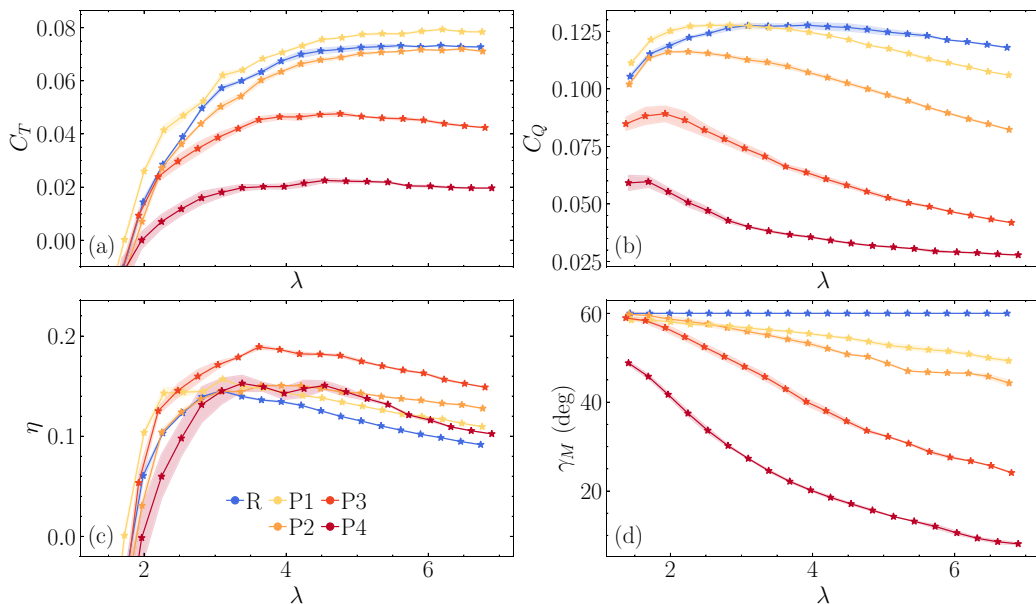


FIG. 3. (a) Thrust coefficient C_T , (b) torque coefficient C_Q , (c) propulsive efficiency η , and (d) tip twist angle γ_M as a function of the tip speed ratio λ . Colors indicate the flexibility of the blades: blue for the rigid ones and yellow to red for increasingly flexible blades. Shaded areas indicate fluctuations between repeated measurements. All the data correspond to a pitch angle $\gamma_0 = 60^\circ$. Flexibility reduces both the thrust and torque produced by the rotor by decreasing the twist angle γ_M and therefore the angle of attack, α . With this particular pitch angle, the effect of this shape change is to improve the propulsive efficiency.

For this particular large pitch angle ($\gamma_0 = 60^\circ$), the reduction of both thrust and torque in comparison with the rigid blades leads to a significant improvement of the global efficiency of the propeller [Fig. 3(c)]. This observation can be understood as follows in the limit of high tip speed ratios: if $R\Omega \gg U_\infty$, then the local flow velocity angle φ [as defined in Fig. 2(b)] approaches zero, meaning that the effective angle of attack, $\alpha = \gamma - \varphi$, is reduced to γ . The global efficiency depends on the lift-to-drag ratio distribution of each blade radial section. If the lift-to-drag ratio is high everywhere on the blade, so will be the efficiency of the propeller. However, the lift-to-drag ratio is the highest for moderate angles of attack: $10^\circ < \alpha_{\text{opt}} < 20^\circ$ (for our geometry and setup, we measured the lift and drag coefficients separately and obtained an optimal angle $\alpha_{\text{opt}} = 17^\circ$). Therefore, for this specific large-pitch-angle case, the angle of attack on the rigid bladed propeller ($\alpha \approx \gamma_0 = 60^\circ$) is too large to generate efficient propulsion. For a flexible bladed propeller, the bending and twisting mechanisms tend to decrease the local angle of attack on the blade, which is almost always beneficial for efficiency. With a right choice of the mechanical properties of the blade, it is possible to find a so-called optimal Cauchy number that maximizes the global efficiency: as can be seen in Fig. 3(c), the red curve (blades P3) is above the most flexible dark red one (blades P4). Of course, if the angle of attack is reduced beyond α_{opt} (i.e., typically if the blades are too deformable), then the efficiency will decrease (summed up in Fig. 4).

The same type of nonmonotonic behavior can also be seen for the thrust coefficient: only the P1 blades produce more thrust than the rigid ones [Fig. 3(a)]. This is due to the fact that the optimal angle of attack for thrust production is $\alpha \approx 45^\circ$. The reduction of angle of attack from 60° for the rigid blades is therefore at first beneficial for thrust before being detrimental for large deflections.

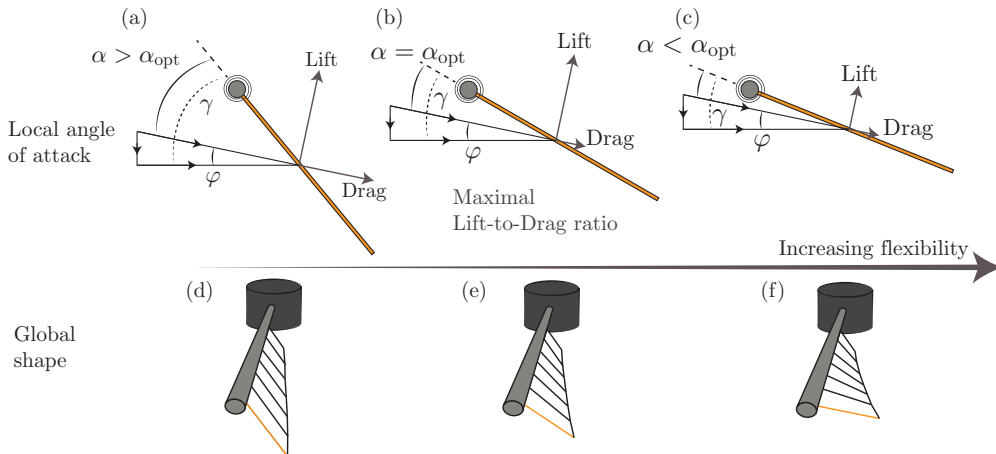


FIG. 4. Schematic of the mechanism that leads to improved efficiency. [(a)–(c)] Evolution of the angle of attack with the material flexibility for one given blade section. [(d)–(f)] Evolution of the global shape of the blade as the deflection is larger at the tip than at the root. In (a) the blade is rigid and the angle of attack, α , is larger than the one maximizing the lift-to-drag ratio: α_{opt} . (b) The effect of flexibility is to reduce the twist angle γ , therefore also reducing α . (c) Extremely flexible blades reduce α to values smaller than α_{opt} , the lift-to-drag ratio is reduced, and there is therefore an optimal flexibility.

IV. EFFICIENCY IMPROVEMENTS

The mechanisms described above can be generalized over a large range of external conditions to compare the efficiency of different propellers.

In Fig. 5(a), the propeller efficiency is shown as a function of the tip speed ratio for the P3 blades (corresponding the highest efficiency case shown in Fig. 3) and a pitch angle ranging from 40° to 60° . In order to compare these different configurations to the rigid case, we also show the efficiency curves of the rigid bladed rotor for the different pitch angles studied (in blue; different pitch angles are identified with different markers). The study of the efficiency curves for the rigid case and for different pitch angles is crucial for the understanding of the efficiency improvement brought using flexible blades.

The efficiency curves for the rigid blades all display a maximum for an intermediate tip speed ratio (except for the case corresponding to $\gamma_0 = 80^\circ$ that remains very inefficient). Connecting all the maxima of the above curves defines a tip-speed-ratio-dependent pitch angle for optimal efficiency (i.e., for a given tip speed ratio λ , the pitch angle is adapted to give the maximal efficiency).

This optimal pitch angle relation as a function of the tip speed ratio $\gamma_0^{opt}(\lambda)$ is shown in Fig. 5(b) and is a decreasing function of the tip speed ratio. In other words, the pitch angle should decrease as λ increases if we want the propeller to keep its best efficiency.

We now understand, for a flexible bladed rotor, how the efficiency of the propellers is closely linked to the twist angle γ along the span as was shown in the schematic of Fig. 4. In principle, the aim is to design a flexible blade that deforms such that the twist angle (or effective pitch angle) γ closely follows the decreasing curve displayed in Fig. 5(b).

This is what we observe if we superimpose in Fig. 5(b) the measured tip twist angle γ_M for the P3 flexible blades with a pitch angle γ_0 ranging from 40° to 60° to the plot (in blue) of $\gamma_0^{opt}(\lambda)$ measured experimentally (i.e., the pitch angle corresponding to the maximum efficiency of the rigid blades for each tip speed ratio). The three curves associated with a high efficiency have a slope that closely follows the evolution of the experimental value of γ_0^{opt} . Comparing these data with those presented in Fig. 3 we see that the other flexible blades cannot reproduce this effect: both the P1

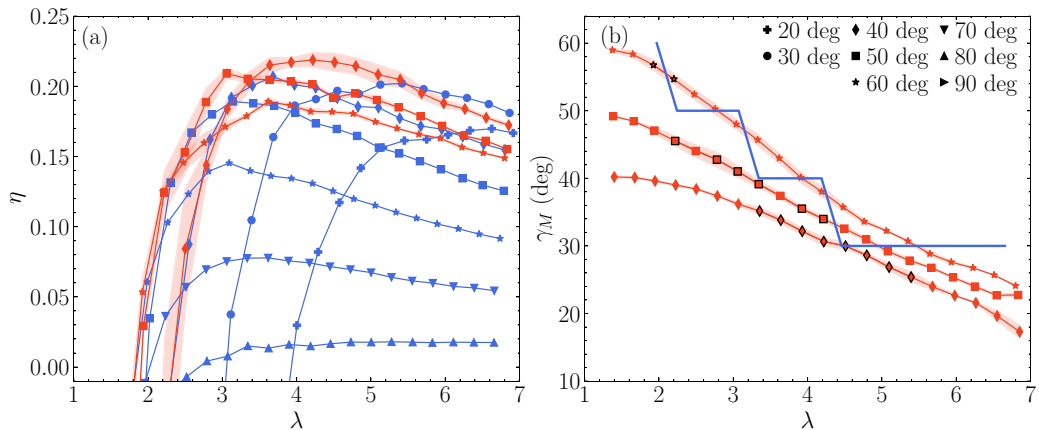


FIG. 5. (a) Efficiency η as a function of the tip speed ratio λ . P3 blades (red) are displayed for $\gamma_0 = 40^\circ$, 50° , and 50° while rigid blades (blue) are displayed as a reference for all pitch angles. Markers represent the pitch angle. Near the optimum, the efficiency curves of these flexible blades are superior to those of the rigid blades. The flexibility allows the propellers to have high efficiency over a wider range of λ . (b) Corresponding tip twist angle. The blue line corresponds to the optimal pitch angle for the rigid blades, $\gamma_0^{\text{opt}}(\lambda)$, measured experimentally. Markers with dark edge colors correspond to data points where the flexible propeller is more efficient than the rigid ones, whichever the pitch angle. Tip twist close to the optimum pitch angle corresponds to high efficiency.

and P2 blades have a slope much smaller than the one needed to follow $\gamma_0^{\text{opt}}(\lambda)$ and the P4 blades deform way too much.

In this work, we see that, depending on the material properties, flexible propellers can passively adapt to changing external conditions by bringing the effective pitch angle close to its optimal value. This is the case, for instance, of the P3 rotor at a pitch angle of 40° that overcomes all the efficiency curves of the rigid case displayed in Fig. 5(a). It is worth noting that the physics described here is based on the blade tip deformation. In itself, each radial section of the optimum shape of the flexible blade should match the local effective pitch angle based on the local tip speed ratio $\lambda(r)$ (as pictured in Fig. 4, bottom row). However, the blade tip region corresponds to the location where most of the force is generated and therefore driving the physics of the propeller.

V. TWIST ANGLE PREDICTION

Tip twist is crucial in predicting the efficiency of a flexible blade. In the following, we therefore focus on predicting its evolution as a function of the pitch angle γ_0 , tip speed ratio λ , and Cauchy number C_γ . First, we derive the equation for the twist angle γ and extract a predictive relationship using a first-order approximation.

For the sake of simplicity, we chose to divide the blade into independent spanwise beams clamped at the leading edge rather than solving the blade shape as a single elastic plate (Fig. 2). This approach has been shown by Cognet [24] to converge to the same solution when the number of beams is increased in the case of wind turbines. This approach neglects the elastic energy associated with the spanwise torsion. However, this energy is always one order of magnitude smaller than the one associated with chordwise bending: the ratio between the two can be approximated as $E_{\text{span}}/E_{\text{chord}} \sim J/(I(1 + \nu_p)(\Delta\varepsilon/\varepsilon \times c/(R - R_{\text{min}}))^2)$, with ν_p the Poisson ratio of the material. I and J are the second moment of area and torsional moduli, respectively (both are the same order of magnitude for elastic ribbons [25]). $\varepsilon = \gamma - \gamma_0$ is the deflection of the blade and $\Delta\varepsilon$ is the difference in deflection between the tip and the root. The chordwise elastic energy is therefore larger than the one associated

to torsion by a factor larger than the square of the aspect ratio. In addition, in our experiments, the torsion is small compared to the bending itself [i.e., $\Delta\varepsilon/\varepsilon \ll 1$; see Fig. 2(a)]. The elastic restoring force associated to each local beam is therefore modeled as a pointwise torsion spring attached to the leading edge [Fig. 2(b)].

We consider a blade section, at a distance r from the axis of rotation. Two terms contribute to the moment balance at the leading edge: the hydrodynamic loading and the elastic restoring torsion moment. The latter reads

$$M_{\text{elastic}} = C(\gamma(r) - \gamma_0). \quad (8)$$

The hydrodynamic contribution is computed dividing the resultant force into lift and drag contributions. The force normal to the blade chord per unit span reads

$$F_{\text{hydro}} = \frac{1}{2}\rho c(U_\infty^2 + (R\Omega)^2)(C_L(\alpha) \cos \alpha + C_D(\alpha) \sin \alpha), \quad (9)$$

where C_L and C_D are the lift and drag coefficients of the blade profile, respectively. We neglect here the effect of the rotor self-induction, which slightly accelerates the fluid upstream before it reaches the rotor. This force is applied at a distance $\delta_{AC}^{LE} = c/4$ from the blade leading edge [26]. The conservation of angular momentum at the blade leading edge reads

$$0 = C(\gamma(r) - \gamma_0) - \frac{1}{2}\rho c(U_\infty^2 + (R\Omega)^2)(C_L(\alpha) \cos \alpha + C_D(\alpha) \sin \alpha)\delta_{AC}^{LE}. \quad (10)$$

Using $R\Omega$ and c as reference velocity and length, respectively, this equation can be written in dimensionless form using the Cauchy number C_Y :

$$\gamma(r) = \gamma_0 - C_Y \left(1 + \frac{1}{\lambda^2}\right) (C_L(\alpha) \cos \alpha + C_D(\alpha) \sin \alpha) \delta_{AC}^{LE}, \quad (11)$$

with $\delta_{AC}^{LE} = \bar{\delta}_{AC}^{LE}/c$. This equation is nonlinear due to the feedback from the hydrodynamic forcing, the angle of attack being $\alpha = \gamma - \varphi$.

We derive a law for small deformations by developing at the first order Eq. (11). The tip deformation $\varepsilon = \gamma_M - \gamma_0$ is considered to be small, and the angle of attack at the tip reads

$$\alpha = \varepsilon + \alpha_0, \quad (12)$$

where $\alpha_0 = \gamma_0 - \arctan 1/\lambda$ is the angle of attack of the undeformed blade. The right-hand-side terms of Eq. (11) then read

$$C_L(\alpha) \cos \alpha \approx C_L(\alpha_0) \cos \alpha_0 + \varepsilon \left(-C_L(\alpha_0) \sin \alpha_0 + \left. \frac{\partial C_L}{\partial \alpha} \right|_{\alpha_0} \cos \alpha_0 \right), \quad (13)$$

$$C_D(\alpha) \sin \alpha \approx C_D(\alpha_0) \sin \alpha_0 + \varepsilon \left(C_D(\alpha_0) \cos \alpha_0 + \left. \frac{\partial C_D}{\partial \alpha} \right|_{\alpha_0} \sin \alpha_0 \right). \quad (14)$$

We obtain the approximated law for the deformation ε :

$$\varepsilon = -C_Y \left(1 + \frac{1}{\lambda^2}\right) \delta_{AC}^{LE} \left(C_N(\alpha_0) + \varepsilon \left. \frac{\partial C_N}{\partial \alpha} \right|_{\alpha_0} \right), \quad (15)$$

where $C_N(\alpha) = C_L(\alpha) \cos \alpha + C_D(\alpha) \sin \alpha$ is the normal force coefficient and

$$\left. \frac{\partial C_N}{\partial \alpha} \right|_{\alpha_0} = -C_L(\alpha_0) \sin \alpha_0 + \left. \frac{\partial C_L}{\partial \alpha} \right|_{\alpha_0} \cos \alpha_0 + C_D(\alpha_0) \cos \alpha_0 + \left. \frac{\partial C_D}{\partial \alpha} \right|_{\alpha_0} \sin \alpha_0. \quad (16)$$

Finally, we obtain the following relationship for the theoretical twist deformation:

$$\varepsilon_{\text{theor}} = -\frac{C_Y(1 + 1/\lambda^2)\delta_{AC}^{LE} C_N(\alpha_0)}{1 + C_Y(1 + 1/\lambda^2)\delta_{AC}^{LE} \left. \frac{\partial C_N}{\partial \alpha} \right|_{\alpha_0}}. \quad (17)$$

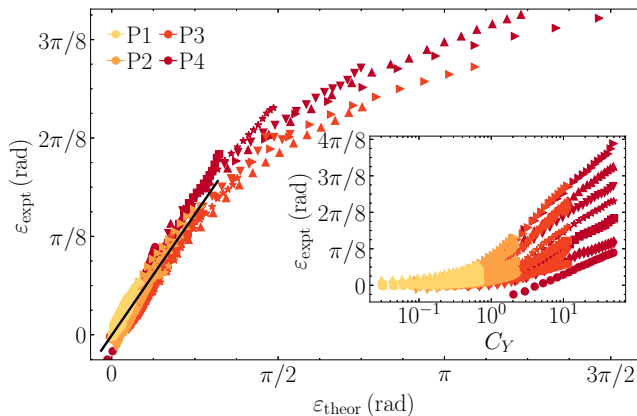


FIG. 6. Blade deformation at the tip $\varepsilon_{\text{expt}}$ as a function of its theoretical expression $\varepsilon_{\text{theor}}$. The data collapse onto a single line of slope 0.65 (black line). Inset: Blade deformation as a function of the Cauchy number alone. Color indicates flexibility and markers indicate the pitch angle similarly to previous plots.

The lift and drag coefficients are computed using a simple flat plate model [10,27]: $C_L(\alpha) = C_L^1 \sin \alpha \cos \alpha$ and $C_D(\alpha) = C_D^0 + C_D^1 \sin^2 \alpha$, with C_L^1 , C_D^0 , C_D^1 constants fitted on measured blade lift and drag coefficients at a similar Reynolds number ($C_L^1 = 1.93$, $C_D^0 = 0.1$, and $C_D^1 = 1.6$). Using these coefficients, we can compute the first-order linearized deformation $\varepsilon_{\text{theor}}$ [note that none of the terms in Eq. (16) is negligible; first-order development is required to capture the deformation of the blades].

The deformation measured experimentally follows a linear trend as predicted by the theory for small deformations (Fig. 6). The slope of this trend is 0.65, and is valid up to a deformation of about 40° . Beyond this value, corresponding to highly flexible and high pitch blades, the slope decreases, but the collapse of the experimental data remains satisfactory. This scaling of the deformation is robust to changes of the exact coefficients used to compute the normal force C_N . We found that variations of 20% in these coefficients still collapse the data, although with a different slope.

VI. CONCLUSION

We studied the deformation and efficiency of a flexible blade propeller, which deforms in response to fluid loading. By choosing the appropriate flexible material, we have shown that the blade deformation maintains a high efficiency even in off-design conditions. The blade shape passively adapts to a changes in tip speed ratio λ and therefore a flexible propeller can be as efficient as the optimal rigid propeller over a wide range of λ (e.g., from $\lambda = 3-5.5$ for $\gamma_0 = 40^\circ$). The following steps should be followed in order to achieve the desired effect for a given geometry: First, it is necessary to compute or measure $\gamma_0^{\text{opt}}(\lambda)$, the optimal pitch angle that maximizes the efficiency of the rigid propeller at a specific λ . Then, based on the linear relationship for moderate deflections from Eq. (17), the deformation of the blade can be predicted given the geometry and blade profile used. Finally, when the deformation matches the evolution $\gamma_0^{\text{opt}}(\lambda)$ (giving the right Cauchy number or material flexibility), the blades will passively adapt to maintain an optimized shape and therefore a high efficiency.

In the specific case of a wind turbine, Cognet *et al.* [10] showed that very similar results can be achieved with one key difference: this configuration has two degrees of freedom to program the deformation of the blade in response to a given load, the flexibility of the material and its density. In contrast to this work, the centrifugal force cannot be neglected in the context of wind turbines and is an additional parameter. However, our results show that by using flexibility as the only parameter

of the system, we can still extend the range of efficient propulsion, with the only difference being the range of tip speed ratio values where high efficiency occurs.

An interesting comparison could be made between the results obtained here and those obtained with a blade where the flexibility is actually concentrated at the leading edge, with the blade made up of independent spanwise rigid plates. Such a blade would eliminate two limiting factors: first, the chordwise curvature of the blades at high deformation, which is detrimental to efficiency. Second, this blade could achieve a significant spanwise torsion, which would improve both maximum efficiency and optimum shape matching over the range of λ . In addition, investigating how the results presented here change in the presence of spanwise torsion in the undeformed configuration would be an important step towards engineering applications.

-
- [1] S. Vogel, Drag and reconfiguration of broad leaves in high winds, *J. Exp. Bot.* **40**, 941 (1989).
 - [2] S. Alben, M. Shelley, and J. Zhang, Drag reduction through self-similar bending of a flexible body, *Nature (London)* **420**, 479 (2002).
 - [3] S. Alben, M. Shelley, and J. Zhang, How flexibility induces streamlining in a two-dimensional flow, *Phys. Fluids* **16**, 1694 (2004).
 - [4] E. de Langre, Effects of wind on plants, *Annu. Rev. Fluid Mech.* **40**, 141 (2008).
 - [5] F. P. Gosselin and E. de Langre, Drag reduction by reconfiguration of a poroelastic system, *J. Fluids Struct.* **27**, 1111 (2011).
 - [6] L. Schouveiler and A. Boudaoud, The rolling up of sheets in a steady flow, *J. Fluid Mech.* **563**, 71 (2006).
 - [7] J. H. Costello, S. P. Colin, B. J. Gemmell, J. O. Dabiri, and E. A. Kanso, A fundamental propulsive mechanism employed by swimmers and flyers throughout the animal kingdom, *J. Exp. Biol.* **226**, jeb245346 (2023).
 - [8] F. E. Fish, M. K. Nusbaum, J. T. Beneski, and D. R. Ketten, Passive cambering and flexible propulsors: Cetacean flukes, *Bioinspir. Biomim.* **1**, S42 (2006).
 - [9] S. Ramananarivo, R. Godoy-Diana, and B. Thiria, Rather than resonance, flapping wing flyers may play on aerodynamics to improve performance, *Proc. Natl. Acad. Sci. USA* **108**, 5964 (2011).
 - [10] V. Cognet, S. Courrech du Pont, I. Dobrev, F. Massouh, and B. Thiria, Bioinspired turbine blades offer new perspectives for wind energy, *Proc. R. Soc. London A* **473**, 20160726 (2017).
 - [11] J. Sicard and J. Sirohi, Experimental study of an extremely flexible rotor for microhelicopters, *J. Aircr.* **49**, 1306 (2012).
 - [12] F. Mohd Zawawi, P. Lv, S. Prothin, J. Morlier, J.-M. Moschetta, and E. Bénard, Study of a flexible UAV proprotor, *Int. J. Eng. Syst. Modell. Simul.* **6**, 149 (2014).
 - [13] S. Hoerner, C. Bonamy, O. Cleynen, T. Maître, and D. Thévenin, Darrieus vertical-axis water turbines: Deformation and force measurements on bioinspired highly flexible blade profiles, *Exp. Fluids* **61**, 141 (2020).
 - [14] P. Lv, S. Prothin, F. Mohd-Zawawi, E. Benard, J. Morlier, and J.-M. Moschetta, Performance improvement of small-scale rotors by passive blade twist control, *J. Fluids Struct.* **55**, 25 (2015).
 - [15] D. W. MacPhee and A. Beyene, Experimental and fluid structure interaction analysis of a morphing wind turbine rotor, *Energy* **90**, 1055 (2015).
 - [16] M. Somoano and F. J. Huera-Huarte, Bio-inspired blades with local trailing edge flexibility increase the efficiency of vertical axis wind turbines, *Energy Rep.* **8**, 3244 (2022).
 - [17] V. Cognet, S. Courrech du Pont, and B. Thiria, Material optimization of flexible blades for wind turbines, *Renewable Energy* **160**, 1373 (2020).
 - [18] T. Aurégan, B. Thiria, and S. Courrech du Pont, Scaling the thrust and deformations of a rotor with flexible blades, *Phys. Rev. Fluids* **8**, 044401 (2023).
 - [19] E. Durán Venegas, S. Le Dizès, and C. Eloy, A strongly-coupled model for flexible rotors, *J. Fluids Struct.* **89**, 219 (2019).

- [20] J. Sicard and J. Sirohi, Aeroelastic stability of a flexible ribbon rotor blade, *J. Fluids Struct.* **67**, 106 (2016).
- [21] A. Eldemerdash and T. Leweke, Fluid–structure interaction of a flexible rotor in water, *J. Fluids Struct.* **103**, 103259 (2021).
- [22] See Supplemental Material at <http://link.aps.org/supplemental/10.1103/PhysRevFluids.9.074402> for details about the experimental setup and numerical analysis of the effect of rotor tilt.
- [23] R. O. Duda and P. E. Hart, Use of the Hough transformation to detect lines and curves in pictures, *Commun. ACM* **15**, 11 (1972).
- [24] V. Cognet, Optimisation des éoliennes à axe horizontal par l’utilisation de pales flexibles, Ph.D. thesis, Université Paris Cité, 2017.
- [25] B. Audoly and Y. Pomeau, *Elasticity and Geometry: From Hair Curls to the Non-linear Response of Shells* (Oxford University Press, Oxford, UK, 2010).
- [26] H. Li, T. Goodwill, Z. Jane Wang, and L. Ristroph, Centre of mass location, flight modes, stability and dynamic modelling of gliders, *J. Fluid Mech.* **937**, A6 (2022).
- [27] W. A. Timmer, Aerodynamic characteristics of wind turbine blade airfoils at high angles of attack, Third EWEA Conference—Torque 2010, European Wind Energy Association (2010), p. 8.